

See discussions, stats, and author profiles for this publication at: <https://www.researchgate.net/publication/230330338>

Computational Chemistry and Molecular Simulations of Phosphoric Acid

ARTICLE *in* INTERNATIONAL JOURNAL OF QUANTUM CHEMISTRY · OCTOBER 2011

Impact Factor: 1.43 · DOI: 10.1002/qua.22702

CITATIONS

4

READS

37

5 AUTHORS, INCLUDING:



Shuo Li

Procter & Gamble

10 PUBLICATIONS 177 CITATIONS

SEE PROFILE



Joel Fried

University of Louisville

145 PUBLICATIONS 1,589 CITATIONS

SEE PROFILE



Douglas Dudis

Wright-Patterson Air Force Base

96 PUBLICATIONS 844 CITATIONS

SEE PROFILE

Computational Chemistry and Molecular Simulations of Phosphoric Acid

SHUO LI,¹ J. R. FRIED,¹ JEREMY SAUER,² JOHN COLEBROOK,³
DOUGLAS S. DUDIS⁴

¹Department of Chemical and Materials Engineering, University of Cincinnati, Cincinnati, OH 45221-0012

²Department of Chemical Engineering, University of Massachusetts (Amherst), MA 01003

³Department of Chemical Engineering, Bucknell University, Lewisburg, PA 17837

⁴Materials and Manufacturing Directorate, Air Force Research Laboratory, Wright Patterson AFB, OH 45433

Received 15 December 2009; accepted 25 February 2010

Published online 22 September 2010 in Wiley Online Library (wileyonlinelibrary.com).

DOI 10.1002/qua.22702

ABSTRACT: Quantum mechanics (QM) calculations, molecular dynamics (MD) simulations using the condensed-phase optimized molecular potentials for atomistic simulation studies (COMPASS) force field, and the atom-centered density matrix propagation (ADMP) approach have been used to investigate properties of phosphoric acid (PA). QM using B3LYP/6-31++G(d,p) density functional theory were used to calculate gas-phase proton affinities and interaction energies of PA and its derivatives. Detailed single coordinate driving, followed by quadratic synchronous transit optimization was used to determine energy barriers for different proton transfer (PT) pathways. Determined energy barrier heights in ascending order are (unit: kJ/mol): $\text{H}_3\text{O}^+ \rightarrow \text{H}_3\text{PO}_4$ (0); $\text{H}_4\text{P}_2\text{O}_7 \rightarrow \text{H}_3\text{PO}_4$ (2.61); $\text{H}_3\text{PO}_4 \rightarrow \text{H}_2\text{PO}_4^-$ (5.31); $\text{H}_4\text{PO}_4^+ \rightarrow \text{H}_3\text{PO}_4$ (~7.33); $\text{H}_3\text{PO}_4 \rightarrow \text{H}_4\text{P}_2\text{O}_7/\text{H}_3\text{PO}_4 \rightarrow \text{H}_3\text{PO}_4$ (15.99); $\text{H}_4\text{P}_2\text{O}_7 \rightarrow \text{H}_2\text{O}$ (28.61); $\text{H}_3\text{PO}_4 \rightarrow \text{H}_2\text{O}$ (47.14). The COMPASS force field was used to study condensed-phase properties of PA. Good agreement between experimental data and MD results including density, radial distribution functions, and self-diffusion coefficient at different temperatures provides validation of the COMPASS force field for PA. Finally, preliminary ADMP studies on a cluster of three PA molecules shows that the ADMP approach can reasonably describe the PT and self-dissociation processes in PA. © 2010 Wiley Periodicals, Inc. *Int J Quantum Chem* 111: 3212–3229, 2011

Key words: phosphoric acid; proton transfer; COMPASS; ADMP; fuel cells

Correspondence to: J. R. Fried; e-mail: joel.fried@uc.edu

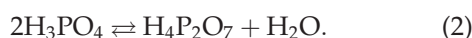
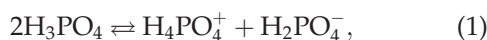
Contract grant sponsor: National Science Foundation (NSF).

Contract grant numbers: EEC Awards #0139438, #0647677.

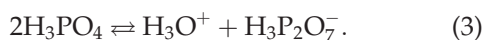
Additional Supporting Information may be found in the online version of this article.

1. Introduction

Phosphoric acid (PA) [H_3PO_4 , Fig. 1(a)] is second to sulfuric acid as the most important inorganic acid, and has great importance in the fertilizer, detergent, and food industries [1, 2]. Above its melting temperature (T_m) of 42 °C, neat PA is a highly viscous liquid with a low self-diffusion coefficient ($1.75 \times 10^{-7} \text{ cm}^2/\text{s}$ at T_m) [3]. Nevertheless, the total conductivity of PA can reach $7.7 \times 10^{-2} \text{ S/cm}$ at T_m , with an estimated proton mobility of $2 \times 10^{-5} \text{ cm}^2/\text{s}$, according to the Nernst–Einstein equation [3, 4]. This high conductivity makes PA suitable for applications as an electrolyte in liquid fuel cells as well as a dopant in polymeric electrolyte membranes (e.g., polybenzimidazoles) [5, 6]. For this reason, understanding the mechanism of proton transfer (PT) in PA and PA-doped systems has great importance. PA has a high degree of self-dissociation (about 7.4% at the T_m) [7], and undergoes dehydration to produce pyrophosphoric acid [PPA, $\text{H}_4\text{P}_2\text{O}_7$, Fig. 1(b)]. The self-dissociation and dehydration reactions can be represented as follows [6, 8]:



PPA is a strong acid and has two dissociation steps to produce the trihydrogen pyrophosphate anion ($\text{H}_3\text{P}_2\text{O}_7^-$) and dihydrogen pyrophosphate anion ($\text{H}_2\text{P}_2\text{O}_7^{2-}$). For this reason, reaction (2) is typically written as [6, 8]



Since the phosphoric to pyrophosphate interconversion is relatively slow and temperature-sensitive, it is difficult to accurately measure the conversion rate experimentally. This makes the PT mechanism in PA difficult to determine.

Several experimental studies have reported physical and transport properties of PA. For example, a density of 1.874 g/cm^3 for neat PA was extrapolated from densities of PA aqueous solutions at room temperature [9]. Neutron diffraction studies have been used to investigate the liquid [10] and crystalline [11] structures of PA. Diffusion coefficients have been determined at different temperatures using the PFG-NMR technique [3].

Spieser et al. [12] have used the Gromos force field to study the structure and diffusional behav-

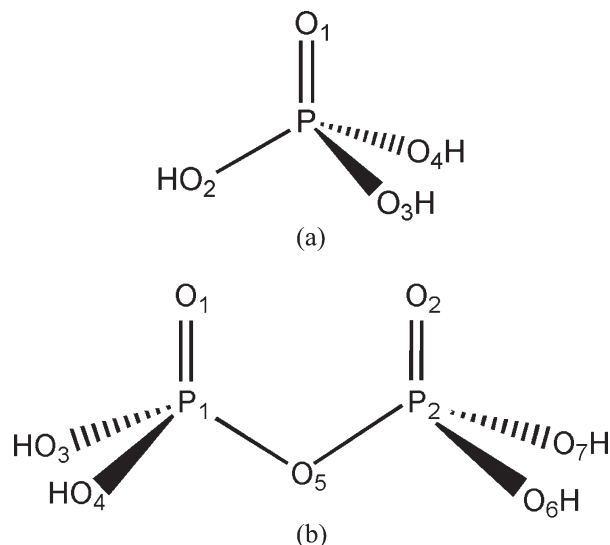


FIGURE 1. Molecular structures of phosphoric acid (a) and pyrophosphoric acid (b).

ior in crystalline PA at 300 K. Density, radial distribution functions (RDFs), and the self-diffusion coefficient reported in that study agreed well with experiment. Tsuchida [13] has used ab initio molecular dynamics (AIMD) methods to investigate the liquid structure of PA at 333 K. The reported RDFs also agreed with the neutron diffraction results. However, the PT mechanisms in PA and PA-doped polymeric electrolyte are not clear.

In the present article, PA has been investigated by a combination of quantum mechanics (QM), molecular dynamics (MD), and AIMD methods. QM methods were used to calculate gas-phase properties of PA and to determine energy barriers for different PT pathways in PA. MD simulations using the condensed-phase optimized molecular potentials for atomistic simulation studies (COMPASS) force field [14, 15] were used to investigate the condensed-phase properties of PA at different temperatures. As traditional MD simulations cannot be used to study the PT phenomena due to their inability to describe bond-breaking and bond-making events, an AIMD method, atom-centered density matrix propagation (ADMP) [16–22], has also been used to investigate the PT process in a cluster of three PA molecules.

2. Computational Methods

2.1. QM CALCULATIONS

All QM calculations were performed using the B3LYP/6-31++G(d,p) level of density functional

theory (DFT) through the Gaussian 03 program package [23]. The gas-phase proton affinities and interaction energies of PA and its derivatives have been calculated. The proton affinity of an anion (A^-) or a neutral molecule (B) is defined as the negative of the enthalpy change at the standard state for the gas phase reaction [24]



The standard state in the gas phase is a mole of particles at 298 K and 1 atm pressure; therefore, the calculated electronic energies of A^- (B) and HA (BH^+) need to be corrected with zero-point energy (ZPE) [25] and thermal enthalpies [26].

The interaction energy E_{int} between two molecules A and B is calculated as the energy difference between the energy of the AB complex and the energies of the isolated components A and B, written as:

$$E_{\text{int}} = E_{\text{AB}} - (E_A + E_B). \quad (5)$$

ZPE corrections [25] and basis set superposition error (BSSE) corrections by the counterpoise approach [27] were used to obtain the final corrected interaction energies.

The single coordinate driving (SCD) technique [28], followed by the quadratic synchronous transit (QST) method (e.g., QST3) [29, 30], was used to determine energy barriers for different PT pathways in PA. In Gaussian03, SCD is a “relaxed scan” process with geometry optimization at each point [23]. All starting geometries were first fully optimized using the B3LYP/6-31++G(d,p) level of DFT. Then SCD was performed also using B3LYP/6-31++G(d,p) DFT along a PT pathway (O \cdots H \cdots O: an intermolecular hydrogen bond) to determine the potential energy profile. The step size of all SCD jobs was chosen between -0.021 and -0.020 Å. The potential energy measured at each point was compared with potential energy of the starting geometry to determine the relative energy change ΔE along the PT trajectory. For structures where a proton can hop back through a second hydrogen bond, additional SCD calculations with constraint added to the length of related intramolecular O—H bonds was performed for comparison. Because of the hysteresis effect of the SCD technique, the determined energy barriers may be inaccurate [31]. For verification, QST3 using B3LYP/6-31++G(d,p) DFT was also used to optimize the “pseudo transition

state” obtained from SCD. With potential energies of the QST-optimized transition states, energy barriers for PT can be calculated and compared with the SCD results.

2.2. MD SIMULATIONS

MD simulations were carried out using the COMPASS force field through Materials Studio 4.3 software [32]. COMPASS [14, 15] is a Class II ab initio force field that derives potential energy terms and some parameters from the consistent force field series of force fields [33, 34] but uses condensed-phase data for final parameterization. As shown by Eq. (6), COMPASS utilizes quartic bond stretch (b) and angle-bend (θ) contributions, three-term Cosine expansions for torsion (Φ), out-of-plane angle (χ), and a number of cross terms for coupled intramolecular interactions in the bonded potential. Non-bonded terms include a Coulombic potential and a 6–9 L-J potential for van der Waals interaction [14].

$$\begin{aligned} E_{\text{total}} = & E_b + E_\theta + E_\phi + E_\chi + E_{b\theta'} + E_{b\theta} + E_{b\phi} + E_{\theta\phi} \\ & + E_{\theta\theta'} + E_{\theta\theta'\phi} + E_{\text{elec}} + E_{\text{LJ}} \\ = & \sum_b \left[K_2(b - b_o)^2 + K_3(b - b_o)^3 + K_4(b - b_o)^4 \right] \\ & + \sum_\theta \left[H_2(\theta - \theta_o)^2 + H_3(\theta - \theta_o)^3 + H_4(\theta - \theta_o)^4 \right] \\ & + \sum_\phi \left[V_1(1 - \cos\phi) + V_2(1 - \cos 2\phi) + V_3(1 - \cos 3\phi) \right] \\ & + \sum_\chi K_\chi(\chi - \chi_o)^2 + \sum_{b,b'} F_{b,b'}(b - b_o)(b' - b'_o) \\ & + \sum_{b,\theta} F_{b,\theta}(b - b_o)(\theta - \theta_o) \\ & + \sum_{b,\phi} (b - b_o) \left[F_{b,\phi}^{(1)} \cos\phi + F_{b,\phi}^{(2)} \cos 2\phi + F_{b,\phi}^{(3)} \cos 3\phi \right] \\ & + \sum_{\theta,\phi} (\theta - \theta_o) \left[F_{\theta,\phi}^{(1)} \cos\phi + F_{\theta,\phi}^{(2)} \cos 2\phi + F_{\theta,\phi}^{(3)} \cos 3\phi \right] \\ & + \sum_{\theta\theta'} F_{\theta,\theta'}(\theta - \theta_o)(\theta' - \theta'_o) \\ & + \sum_{\theta,\theta',\phi} F_{\theta,\theta',\phi}(\theta - \theta_o)(\theta' - \theta'_o) \cos(\phi - \phi_o) \\ & + \sum_{i,j} \frac{q_i q_j}{r_{ij}} + \sum_{i,j} \varepsilon_{ij} \left[2 \left(\frac{r_{ij}^o}{r_{ij}} \right)^9 - 3 \left(\frac{r_{ij}^o}{r_{ij}} \right)^6 \right]. \quad (6) \end{aligned}$$

Amorphous cells (ACs) were constructed using 125 PA molecules (1000 atoms) at an initial density of 1.8 g/cm^3 . This was followed by AC minimization, 50-ps equilibration with the NVT

ensemble, 150-ps NPT dynamics, and finally 3-ns NVT dynamics using COMPASS. PA is a liquid above 333 K. The typical working temperature range of the PA-doped polymeric electrolytes (e.g., polybenzimidazole) is in the range of 393–473 K. As a result, a series of dynamics runs at different simulation temperatures (298, 333, 393, 423, and 453 K) were carried out using the Andersen thermostat [35]. Pressure scaling was performed at a constant pressure of 1 atm using the Berendsen barostat [36]. Except for periodic boundary conditions, there were no additional symmetry constraints. The time step for dynamics used 1 fs. Standard Ewald summation [37] was utilized for both van der Waals and Coulombic interactions.

At the end of 150-ps NPT dynamics, cell density, solubility parameter, and RDFs were analyzed. The solubility parameter was taken as the square root of the cohesive energy density. The self-diffusion coefficient, D , was determined from NVT dynamics using the Einstein equation [38] in the form [39]

$$D = \lim_{t \rightarrow \infty} \frac{1}{6t} \langle |r(t) - r(0)|^2 \rangle, \quad (7)$$

where $\langle |r(t) - r(0)|^2 \rangle$ is the mean square displacement (MSD), $r(t) - r(0)$ is the vector distance traveled by particles over the time interval of length t , and the squared magnitude of this vector is averaged (as indicated by the angle brackets) over many such time intervals. The self-diffusion coefficient was calculated as 1/6 the slope of the MSD versus t plot, for time intervals during which the log-log plot of MSD versus t is in the linear regime with a slope near unity. The activation energy (E_a) for diffusion of PA was calculated from the Arrhenius equation [24]

$$D = D_0 e^{-E_a/RT}. \quad (8)$$

2.3. ATOM-CENTERED DENSITY MATRIX PROPAGATION

ADMP uses an extended Lagrangian molecular dynamic trajectory method to propagate the density matrix in a basis of atom-centered Gaussian functions [16–22]. In an orthonormal basis, ADMP, an extended Lagrangian for the system can be written as [16]

$$L = \frac{1}{2} \text{Tr}(V^T M V) + \frac{1}{2} \mu \text{Tr}(W W) - E(R, P) - \text{Tr}[\Lambda(PP - P)], \quad (9)$$

where M , R , V , P , W , and μ are the nuclear masses, nuclear positions, nuclear velocities, density matrix, density matrix velocity, and the fictitious mass for the electronic degrees of freedom, respectively. Λ is a Lagrangian multiplier matrix that imposes constraints on the total number of electrons and on the idempotency of the density matrix. The advantages of ADMP over other AIMD methods, such as the Car–Parinello method [40], includes of $O(N)$ scaling of computational time with system size [16, 19]. ADMP can also use accurate and effective exchange-correlation functionals, including hybrid density functionals, such as B3LYP, to achieve better accuracy in describing hydrogen-bonded system [22].

Preliminary ADMP calculations on a cluster of three PA molecules were performed for 1 ps using the B3LYP/6-31++G(d,p) DFT method through Gaussian 03 program package [23]. Before the ADMP runs, the starting geometry of the PA cluster was optimized using B3LYP/6-31++G(d,p). The temperature during the simulations was 298 K, enforced by velocity scaling. A time step of 0.25 fs, a fictitious electronic mass of 180 a.u., and a tensorial mass-weighting scheme were used.

3. Results and Discussion

3.1. QM CALCULATIONS

3.1.1. Proton Affinities

Table I lists calculated proton affinities using B3LYP/6-31++G(d,p) for various components in PA. Comparing the proton affinities helps to sort various PA components based on their ability to associate a proton and release the proton after protonation. Generally, the larger the proton affinity, the more prone this component is to associate proton. Results predict proton affinities of various PA components corrected for ZPE and thermal enthalpies in descending order (unit: kJ/mol): $\text{P}_2\text{O}_7^{4-}$ (2584.45) > PO_4^{3-} (2404.41) > $\text{HP}_2\text{O}_7^{3-}$ (2165.65, 2091.78) > HPO_4^{2-} (1892.42) > $\text{H}_2\text{P}_2\text{O}_7^{2-}$ (1667.06, 1740.93) > H_2PO_4^- (1359.76) > $\text{H}_3\text{P}_2\text{O}_7^-$ (1242.38) > $\text{H}_4\text{P}_2\text{O}_7$ (857.45) > H_3PO_4 (822.43) > H_2O (684.12) > $\text{H}_5\text{P}_2\text{O}_7^+$ (434.85). It can be seen that the calculated proton affinity for water is 684.12 kJ/mol, which agrees well with the reported experimental value of 691 kJ/mol [41]. As presented in footnote d of Table I, $\text{H}_2\text{P}_2\text{O}_7^{2-}$ has two different conformers based on optimization

TABLE I

Calculated proton affinities using B3LYP/6-31++G(d,p) for various components in PA. [Color figure can be viewed in the online issue, which is available at [wileyonlinelibrary.com](http://www.wileyonlinelibrary.com).]

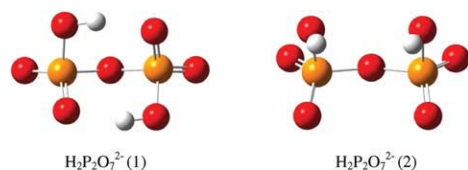
Molecule	E_{elec}^a	$E_{\text{elec}} + \text{ZPE}^b$	H^c	Proton affinity (kJ/mol)
H ₂ O	−76.434123	−76.412856	−76.409076	684.12
H ₃ O ⁺	−76.706153	−76.673427	−76.669644	–
PO ₄ ^{3−}	−641.981275	−641.968710	−641.963235	2404.41
HPO ₄ ^{2−}	−642.908735	−642.884571	−642.879028	1892.42
H ₂ PO ₄ [−]	−643.643109	−643.606576	−643.599814	1359.76
H ₃ PO ₄	−644.173215	−644.124967	−644.117721	822.43
H ₄ PO ₄ ⁺	−644.497703	−644.438289	−644.430968	–
P ₂ O ₇ ^{4−}	−1208.933529	−1208.908288	−1208.899060	2584.48
HP ₂ O ₇ ^{3−}	−1209.931361	−1209.893146	−1209.883435	2165.65 (1) ^d
				2091.78 (2) ^d
H ₂ P ₂ O ₇ ^{2−} (1) ^d	−1210.770030	−1210.717753	−1210.708288	1667.06
H ₂ P ₂ O ₇ ^{2−} (2) ^d	−1210.739348	−1210.689630	−1210.680153	1740.93
H ₃ P ₂ O ₇ [−]	−1211.415944	−1211.354030	−1211.343237	1242.38
H ₄ P ₂ O ₇	−1211.901000	−1211.827940	−1211.816436	857.45
H ₅ P ₂ O ₇ ⁺	−1212.239482	−1212.154941	−1212.143023	434.85
H ₆ P ₂ O ₇ ²⁺	−1212.414856	−1212.320721	−1212.308649	–

^aElectronic energy E_{elec} in Hartrees.

^bElectronic energy with ZPE correction ($E_{\text{elec}} + \text{ZPE}$) in Hartrees.

^cSum of electronic and thermal enthalpies H at 298 K and 1 atm in Hartrees.

^dBased on the optimization results, H₂P₂O₇^{2−} has two different conformers.



*Experimental measured proton affinity for water is 691 kJ/mol, Ref. [41]; 1 Hartree = 2625.5 kJ/mol.

results. Because of the existence of H₂P₂O₇^{2−} conformers, there are two proton affinity values for both H₂P₂O₇^{2−} and HP₂O₇^{3−}, as shown in Table I.

3.1.2. Interaction Energies

Interaction energies with ZPE and BSSE corrections between PA, PPA, and water, calculated at the B3LYP/6-31++G(d,p) level, are given in Table II. The larger the interaction energy, the more prone are the molecules to form hydrogen-bonded molecular pair. Because of the ability to form three intermolecular hydrogen bonds, the PPA-PA pair exhibits the largest interaction energy (129.56 kJ/mol), followed by the PPA-water pair (86.21 kJ/mol), and the PA-PA pair (84.70 kJ/mol). The PA-water pair shows the smallest interaction energy of 38.35 kJ/mol.

3.1.3. Energy Barriers for Different PT Pathways

The relative energy profiles for different PT pathways obtained by the SCD technique at the B3LYP/6-31++G(d,p) level, accompanied by corresponding starting and final geometries are presented in Figures 2–5. Directions of PT are indicated by arrows in both relative energy profiles and starting geometries. The structural parameters during PT are also illustrated in Figures S1–S4 of the Supporting Information.

Figure 2 shows results on PT between PA and PA/phosphate ions. Specifically, PT from phosphate cation (H₄PO₄⁺) to PA (Case 1), PT between two PA molecules (Case 2), PT from PA to phosphate anion (H₂PO₄[−]) (Case 3), and PT from phosphate anion to PA (Case 4) are studied. As illustrated by the starting geometry of the phosphate

TABLE II

Interaction energies E_{int} between PA, PPA, and water, calculated using B3LYP/6-31++G(d,p).

	$E_{\text{elec}}^{\text{a}}$	$E_{\text{elec}} + \text{ZPE}^{\text{b}}$	$E_{\text{elec}} + \text{ZPE} + \text{BSSE}^{\text{c}}$	E_{int} (kJ/mol)
water	-76.434123	-76.412856	—	—
PA	-644.173213	-644.124901	—	—
PPA	-1211.901000	-1211.827938	—	—
PA-water	-720.627901	-720.554175	-720.552363	38.35
PA-PA	-1288.383198	-1288.284805	-1288.282061	84.70
PPA-water	-1288.376054	-1288.276349	-1288.273630	86.21
PA-PPA	-1856.131130	-1856.007112	-1856.002184	129.56

^aTotal electronic energy in Hartrees.^bTotal electronic energy corrected for ZPE in Hartrees.^cTotal electronic energy corrected for both ZPE and BSSE in Hartrees.

cation-PA complex (Case 1), the extra proton lies at the center of symmetry of the two PA molecules. A monotonically increasing energy curve is expected no matter which direction this proton moves toward. The energy curve of Case (1, constraint-free) displays the highest relative potential energy of 7.33 kJ/mol as the $^{15}\text{O}, ^{16}\text{H}\cdots^2\text{O}$ distance decreases to 1.01 Å. Comparing the starting and final geometries of the constraint-free PA-PA complex (Case 2) leads to the conclusion that there is a second proton hopping back through another intermolecular hydrogen bond (^6H transfers from ^5O to ^{10}O). This explains the divergence of relative energy curves of Case (2, constrained) and Case (2, constraint-free) after the $^{15}\text{O}, ^{16}\text{H}\cdots^2\text{O}$ distance decreases below ~ 1.20 Å. The constraint-free relative energy curve of Case 2 shows an energy barrier height of 15.96 kJ/mol at the $^{15}\text{O}, ^{16}\text{H}\cdots^2\text{O}$ distance of 1.19 Å. The relative potential energy of Case (2, constrained) finally reaches 43.95 kJ/mol at 1.01 Å, which is too large to appear in the relative energy profile of Figure 2. For PT between PA and phosphate anion, there are two PT pathways. One is from PA to phosphate anion (Case 3), and the other is from phosphate anion to PA (Case 4). From the constraint-free relative energy curves of Cases 3 and 4, it can be seen that the energy barrier for PT from PA to phosphate anion is 5.45 kJ/mol at the $^7\text{O}, ^8\text{H}\cdots^{11}\text{O}$ distance of 1.21 Å, whereas PT from phosphate anion to PA shows a much higher energy barrier of 25.70 kJ/mol at the $^{14}\text{O}, ^{15}\text{H}\cdots^2\text{O}$ distance of 1.35 Å. The final geometry of Case (3, constraint-free) displays that the $^{14}\text{O}-^{15}\text{H}$ distance is elongated but ^{15}H has not transferred to ^2O . This explains the similarity of the constraint-free and constrained relative energy curves for

Case 3. The final geometry of Case (4, constraint-free) shows a second proton hopping back (^6H transfers from ^5O to ^{10}O). This explains the large energy drop at the $^{14}\text{O}, ^{15}\text{H}\cdots^2\text{O}$ distance of 1.35 Å. As shown by the constraint-free relative energy curve for Cases 3 and 4, after the energy drop, Case (4, constraint-free) becomes Case (3, constraint-free) and undergoes the same relative potential energy change as Case (3, constraint-free) does.

Figure 3 displays results on PT from PA/phosphate cation to water. The relative energy profile in Figure 3 includes three curves for constraint-free PT from phosphate cation to water (Case 1, constraint-free), constraint-free PT from PA to water (Case 2, constraint-free), and constrained PT from PA to water (Case 2, constrained), respectively. It is worthy to note that for PT from hydronium ion (H_3O^+) to PA, which is not displayed in Figure 3, the extra proton on water moves to PA after the initial optimization. This phenomena agrees with the proton affinity result in Section 3.1.1 that the proton affinity of H_3PO_4 (822.43 kJ/mol) is greater than that of H_2O (684.12 kJ/mol) and suggests a no-barrier PT. As shown by the relative energy curve of Case (1, constraint-free) in Figure 3, the extra proton transferring from phosphate cation to water has a monotonically increasing relative potential energy, finally reaching 40.59 kJ/mol as the $^8\text{O}, ^{11}\text{H}\cdots^9\text{O}$ distance decreased to 0.99 Å. For the constraint-free PT from PA to water (Case 2, constraint-free), an energy barrier of 47.15 kJ/mol was obtained at the $^4\text{O}, ^5\text{H}\cdots^9\text{O}$ distance of 1.13 Å, together with a second proton hopping back through another intermolecular hydrogen bond (^{11}H transfers from ^9O to ^8O).

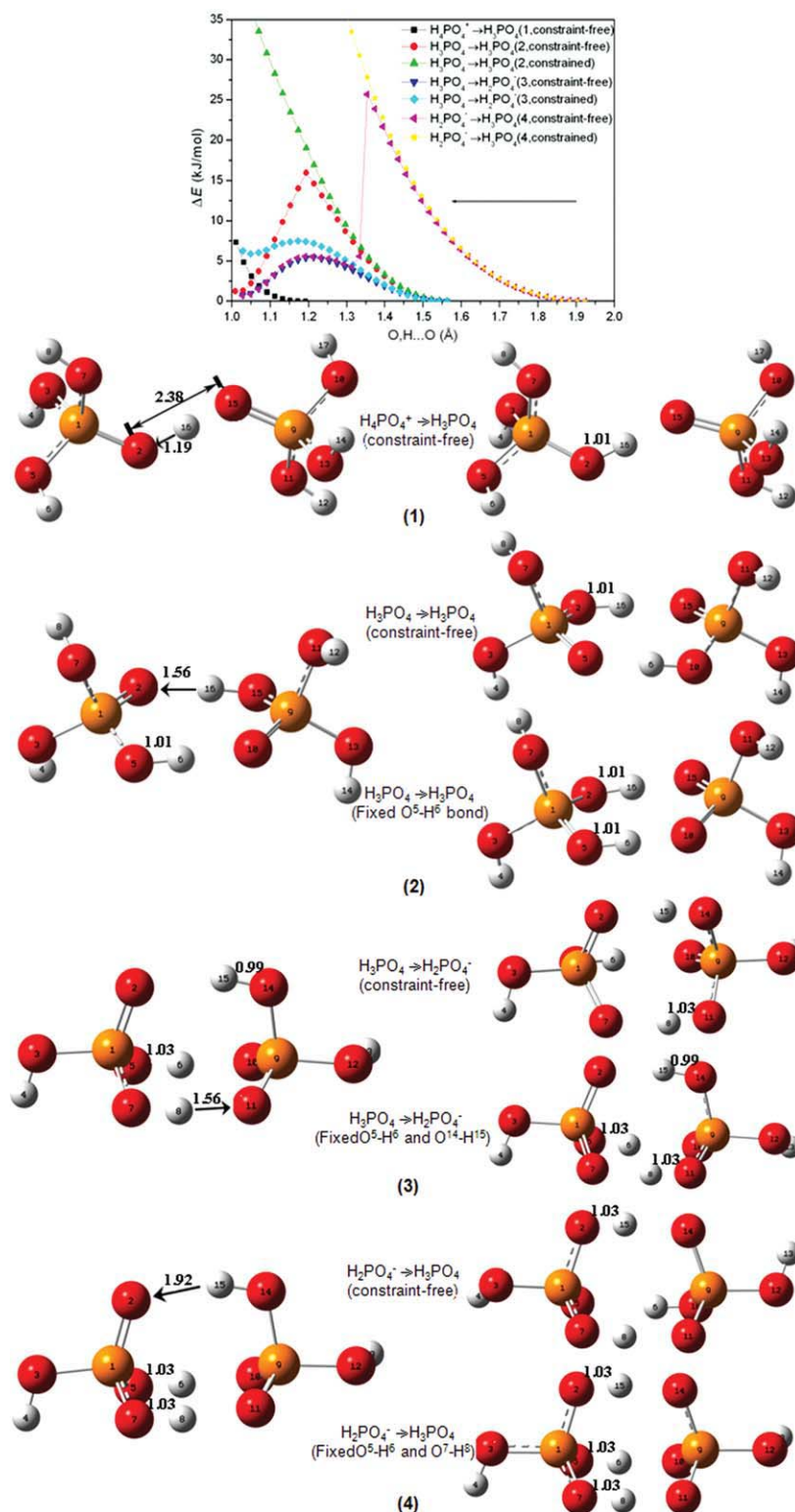


FIGURE 2. Relative energy profile for PT between PA and PA/phosphate ions obtained from SCD results using B3LYP/6-31++G(d,p) DFT, followed by the corresponding starting and final geometries illustrated on the left and right, respectively (arrows indicate the PT direction): (1) $\text{H}_4\text{PO}_4^+ \rightarrow \text{H}_3\text{PO}_4$; (2) $\text{H}_3\text{PO}_4 \rightarrow \text{H}_2\text{PO}_4^-$; (3) $\text{H}_2\text{PO}_4^- \rightarrow \text{HPO}_4^{2-}$; (4) $\text{HPO}_4^{2-} \rightarrow \text{PO}_4^{3-}$. [Color figure can be viewed in the online issue, which is available at wileyonlinelibrary.com.]

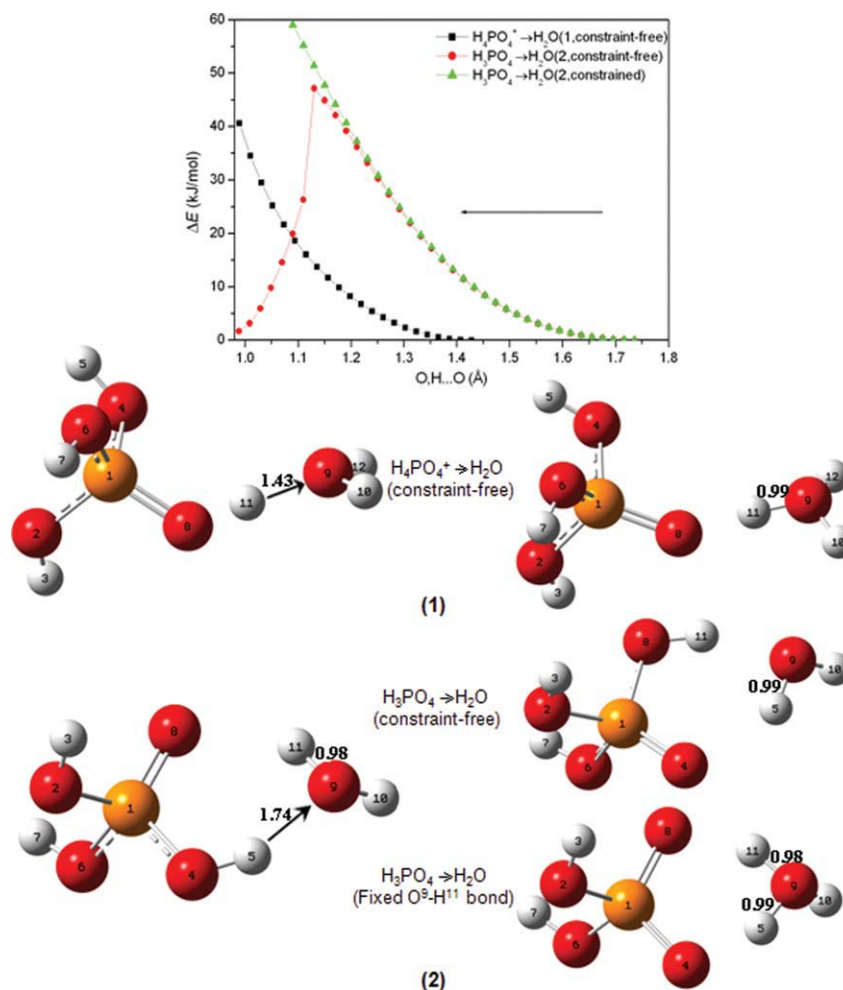


FIGURE 3. Relative energy profile for PT from PA/phosphate cation to water obtained from SCD results using B3LYP/6-31++G(d,p) DFT, followed by the corresponding starting and final geometries illustrated on the left and right, respectively (arrows indicate the PT direction): (1) $\text{H}_4\text{PO}_4^+ \rightarrow \text{H}_2\text{O}$; (2) $\text{H}_3\text{PO}_4 \rightarrow \text{H}_2\text{O}$. [Color figure can be viewed in the online issue, which is available at wileyonlinelibrary.com.]

Figure 4 illustrates results on PT along three intermolecular hydrogen bonds ($\text{O}-\text{H}\cdots\text{O}=\text{P}$) between PPA and PA. For Cases 1 and 2, PTs from PA to PPA; for Case 3, the transferred proton is provided by PPA and PA contributes the double bond oxygen as proton acceptor. The starting geometry of the PPA-PA complex shows that the $^3\text{O}-^6\text{H}$ bond has already been elongated comparing to bond lengths of $^{17}\text{O}-^{18}\text{H}$ and $^{19}\text{O}-^{20}\text{H}$, which suggests the ^{21}O atom on PA is more prone to attract proton than a single ^2O or ^9O atom on PPA. As presented by the final geometries of the constraint-free cases, a second proton hopping back through another hydrogen bond (^6H transfers from ^3O to ^{21}O) occurs in Cases 1 and 2; although in Case 3, the two bond lengths of

$^{17}\text{O}-^{18}\text{H}$ and $^{19}\text{O}-^{20}\text{H}$ are both elongated, but no second proton hopping back occurs, which explains the less obvious divergence between the constrained and constraint-free curves for Case 3 than that for Cases 1 and 2. In the relative energy profile, four curves for Cases 1 and 2 exhibit higher relative potential energy than those two curves for Case 3 throughout the PT process, indicating PT from PPA to PA is more preferred than that from PA to PPA. Specifically, a low energy barrier of 2.91 kJ/mol for PT from PPA to PA (Case 3, constraint-free) was obtained at the $^3\text{O}, ^6\text{H}\cdots^{21}\text{O}$ distance of 1.15 Å. Both local maximum energy of 5.25 kJ/mol at the $^{19}\text{O}, ^{20}\text{H}\cdots^2\text{O}$ distance of 1.50 Å for Case (1, constraint-free) and local maximum energy of 11.24 kJ/mol at the

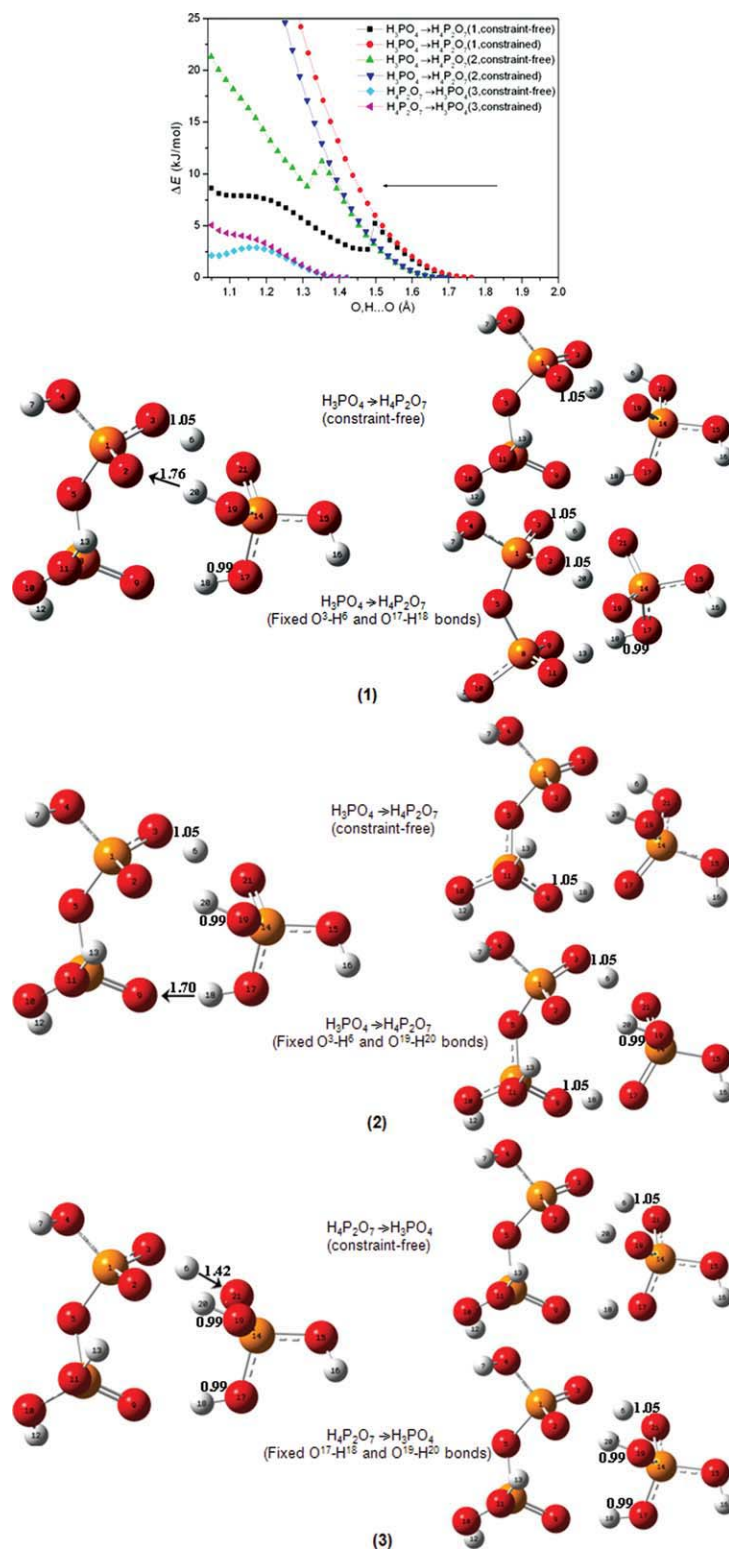


FIGURE 4. Relative energy profile for PT along three intermolecular hydrogen bonds between PPA and PA, obtained from SCD results using B3LYP/6-31++G(d,p) DFT, followed by the corresponding starting and final geometries illustrated on the left and right, respectively (arrows indicate the PT direction): (1, 2) $\text{H}_3\text{PO}_4 \rightarrow \text{H}_4\text{P}_2\text{O}_7$; (3) $\text{H}_4\text{P}_2\text{O}_7 \rightarrow \text{H}_3\text{PO}_4$. [Color figure can be viewed in the online issue, which is available at wileyonlinelibrary.com.]

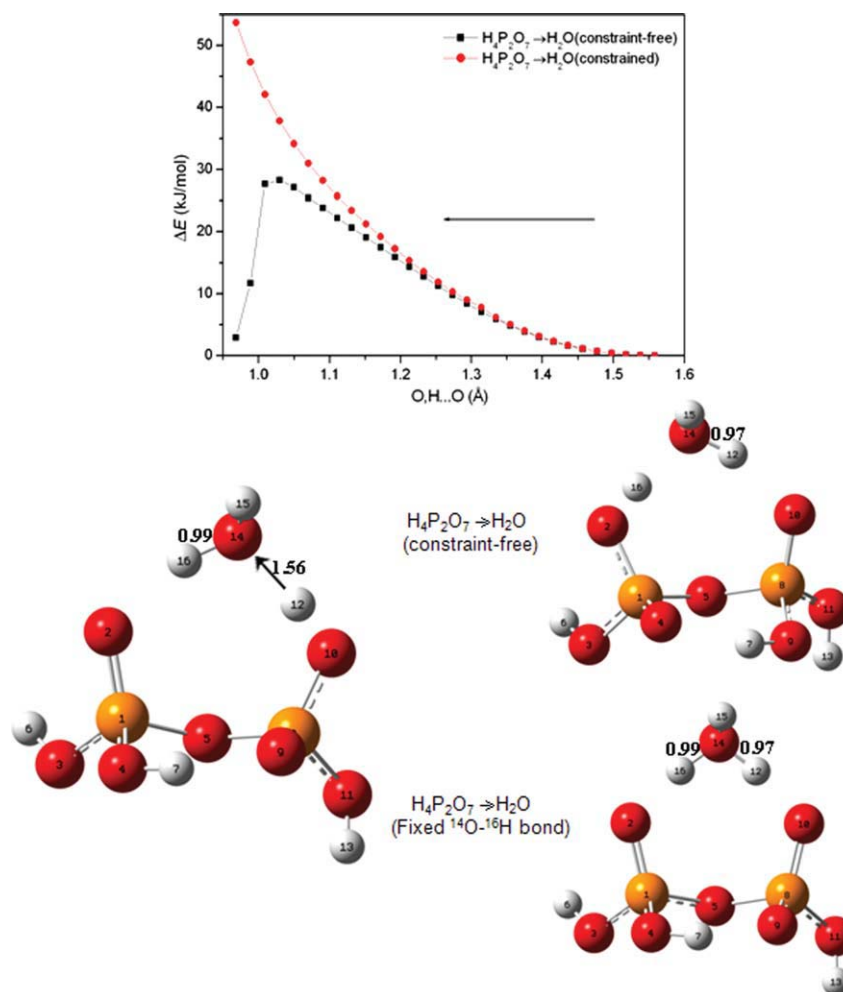


FIGURE 5. Relative energy profile for PT from PPA to water obtained from SCD results using B3LYP/6-31++G(d,p) DFT, followed by the corresponding starting and final geometries illustrated on the left and right, respectively (arrows indicate the PT direction). [Color figure can be viewed in the online issue, which is available at wileyonlinelibrary.com.]

$^{17}\text{O}, ^{18}\text{H} \cdots ^9\text{O}$ distance of 1.35 Å for Case (2, constraint-free) correspond to a second proton hopping back. But in Cases 1 and 2, the energies continue to increase as the O,H...O distance further decreases. At 1.05 Å, the relative energies for Cases 1 and 2 reach 8.64 and 21.32 kJ/mol, respectively. These results can also be explained by previous proton affinity results that the proton affinity of H_2PO_4^- (1359.76 kJ/mol) is greater than that of $\text{H}_3\text{P}_2\text{O}_7^-$ (1242.38 kJ/mol), which means the $\text{H}_3\text{P}_2\text{O}_7^-$ ion can provide quite limited energy for a proton to jump over the energy barrier and bond to it, especially for the two-hydrogen-bond situation.

Figure 5 depict PT from PPA to water. The constraint-free relative energy curve shows an

energy barrier of 28.28 kJ/mol at the $^{10}\text{O}, ^{12}\text{H} \cdots ^{14}\text{O}$ distance of 1.03 Å, accompanied by a second proton hopping back through another hydrogen bond (^{16}H transfers from ^{14}O to ^2O). The relative potential energy for constrained PT reaches 53.70 kJ/mol at the $^{10}\text{O}, ^{12}\text{H} \cdots ^{14}\text{O}$ distance of 0.97 Å.

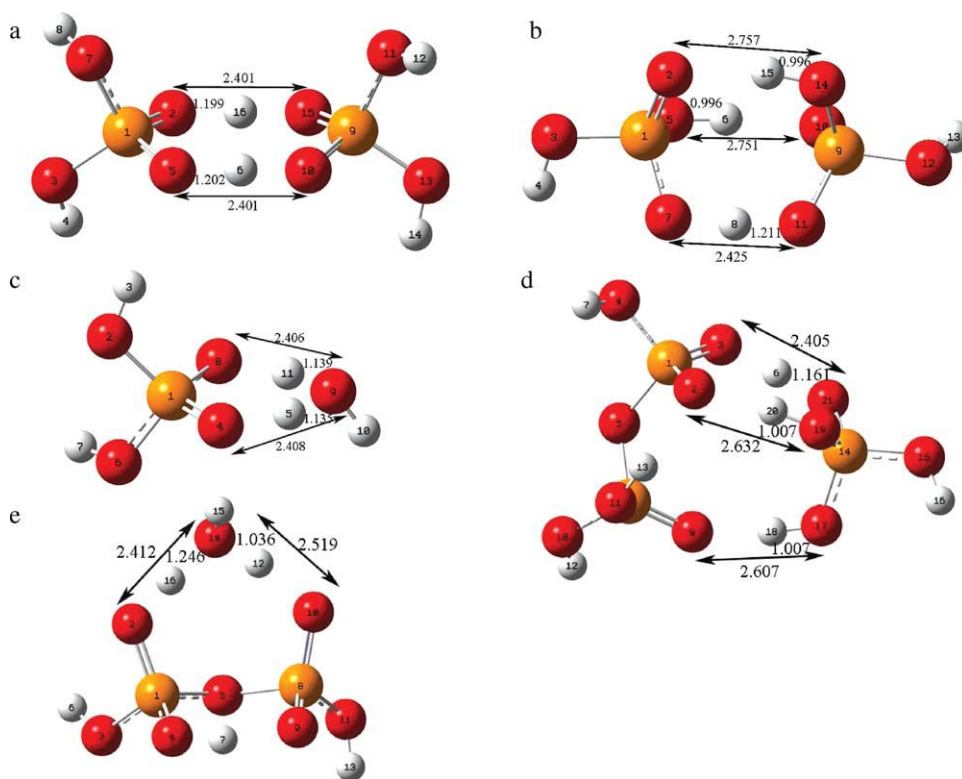
As introduced in the Section 2.1, the determined energy barriers by the SCD technique may be inaccurate because of the hysteresis effect [31], and QST3 was utilized to further optimize the “pseudo transition state” obtained from SCD for verification. The energy barriers and corresponding O,H...O distances determined by SCD and QST3 techniques, together with the optimized transition state structures using QST3, are summarized in Table III. Results indicate that the SCD

TABLE III

Energy barriers for different PT pathways and the corresponding (O,H...O) distance, predicted by the SCD technique and QST3 optimization, both using B3LYP/6-31++G(d,p). [Color figure can be viewed in the online issue, which is available at wileyonlinelibrary.com.]

PT pathways	SCD*		QST3	
	O,H...O distance (Å)	Energy barrier (kJ/mol)	O,H...O distance (Å)	Energy barrier (kJ/mol)
Figure 2	$\text{H}_4\text{PO}_4^+ \rightarrow \text{H}_3\text{PO}_4(1)$	1.01	7.33	—
	$\text{H}_3\text{PO}_4 \rightarrow \text{H}_3\text{PO}_4(2)$	1.19 [1.01]	15.96 [43.95]	1.199 ^a
	$\text{H}_3\text{PO}_4 \rightarrow \text{H}_2\text{PO}_4^-(3)$	1.21 [1.17]	5.45 [7.49]	1.211 ^b
	$\text{H}_2\text{PO}_4^- \rightarrow \text{H}_3\text{PO}_4(4)$	1.35 [1.03]	25.70 [82.24]	—
Figure 3	$\text{H}_3\text{O}^+ \rightarrow \text{H}_3\text{PO}_4$	—	0	—
	$\text{H}_4\text{PO}_4^+ \rightarrow \text{H}_2\text{O}(1)$	0.99	40.59	—
	$\text{H}_3\text{PO}_4 \rightarrow \text{H}_2\text{O}(2)$	1.13 [0.99]	47.15 [82.15]	1.135 ^c
Figure 4	$\text{H}_3\text{PO}_4 \rightarrow \text{H}_4\text{P}_2\text{O}_7(1)$	1.05 [1.09]	8.64 [56.66]	—
	$\text{H}_3\text{PO}_4 \rightarrow \text{H}_4\text{P}_2\text{O}_7(2)$	1.05 [1.05]	21.32 [58.80]	—
	$\text{H}_4\text{P}_2\text{O}_7 \rightarrow \text{H}_3\text{PO}_4(3)$	1.15 [1.05]	2.91 [5.08]	1.161 ^d
Figure 5	$\text{H}_4\text{P}_2\text{O}_7 \rightarrow \text{H}_2\text{O}$	1.03 [0.97]	28.28 [53.70]	1.036 ^e

* Data in the square brackets are results of SCD with constraint.*



outcomes agree well with those from QST3, and the hysteresis effect is not serious in this study. Generally, the lower the energy barrier, the easier PT can occur. It can be seen that besides the nearly no-barrier PT from hydronium ion to PA,

PT from PPA to PA has the lowest energy barrier of 2.61 kJ/mol (QST3), followed by 5.31 kJ/mol (QST3) for PT from PA to phosphate anion and ~7.33 kJ/mol (SCD) for PT from phosphate cation to PA. As illustrated by Figures 2–5, constraint-

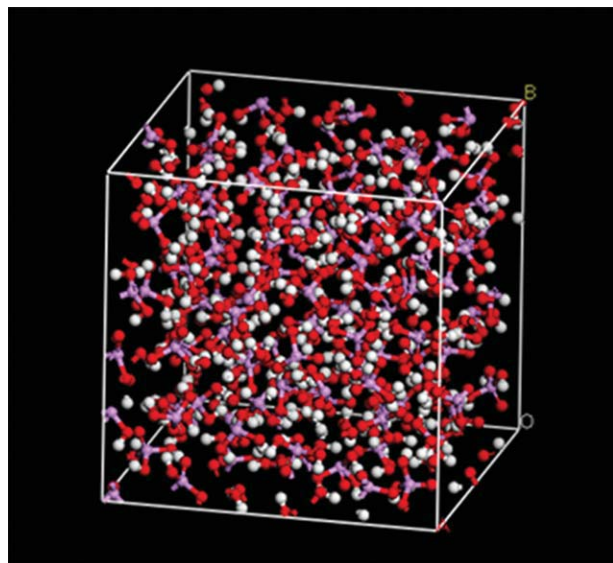


FIGURE 6. The last frame of the 125-molecule PA cell after the final 3-ns NVT dynamics at 298 K. [Color figure can be viewed in the online issue, which is available at wileyonlinelibrary.com.]

free PTs from PA to PA, from PA to water, from PA to PPA, and from PPA to water are all accompanied by a second proton hopping back. By comparing energy barriers for constraint-free/constrained PT and energy barriers determined by QST3 optimization among these neutral systems, it can be concluded that PT from PA to PA

and PT from PA to PPA have comparably low energy barriers (15.99 kJ/mol for PT from PA to PA), followed by PT from PPA to water (28.61 kJ/mol) and PT from PA to water (47.14 kJ/mol). These three energy barriers listed in parentheses are all based on results from QST3 optimization.

3.2. MD SIMULATIONS USING COMPASS

3.2.1. Density

The last frame of the 125-molecule PA cell after the 3-ns NVT dynamics at 298 K is shown in Figure 6. Cell densities simulated at different temperatures are presented in Table IV. Experimentally, a density of 1.874 g/cm³ measured by extrapolation has been reported for liquid (100%) PA at 298 K [9]. This density is 12.96% smaller than the simulation result of 2.153 g/cm³ at 298 K. As explained by reactions [1–3] in the Introduction section, PA has strong self-dissociation and dehydration, especially under a high-concentration condition. Therefore, pure PA that contains only H₃PO₄ molecules does not exist. This may relate to the difference between the experimental density and the simulation result. Besides, simulated densities at 333, 393, 423, and 453 K are 2.120, 2.047, 2.011, and 1.959 g/cm³, respectively. The dependence of the reciprocal of density against temperature in the range 298–453 K is nearly linear.

TABLE IV
Cell densities of the 125-molecule PA cell at different temperatures.

	125 PA 298 K	125 PA 333 K	125 PA 393 K	125 PA 423 K	125 PA 453 K	Exp. 298 K
Density (g/cm ³)	2.153	2.120	2.047	2.011	1.959	1.874 ^a
Standard deviation	0.0001	0.0014	0.0013	0.0013	0.0018	–

^a Experimentally measured density of the pure PA at 298 K, Ref. [9].

TABLE V
Solubility parameters of the 125-molecule PA cell at different temperatures.

	125 PA 298 K	125 PA 333 K	125 PA 393 K	125 PA 423 K	125 PA 453 K	125 water 298 K	Exp. water
Solubility parameter (MPa ^{1/2})	44.65	43.28	39.48	38.26	34.62	48.12	47.9 ^a
Standard deviation	0.294	0.340	0.705	0.637	0.620	0.580	–

^a Experimentally measured solubility parameter of water at 298 K, Ref. [41].

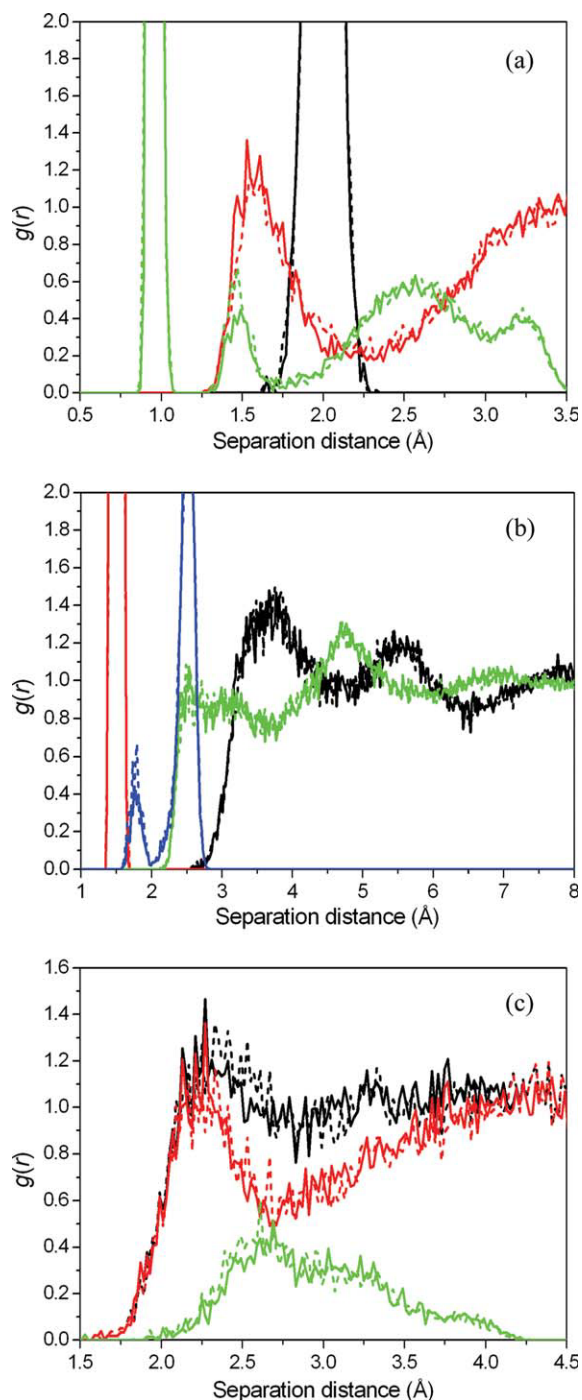


FIGURE 7. The schematic RDFs $g(r)$ for all atom-atom pairs determined at 298 K (full line) and at 333 K (short dashed line). (a) P–H intramolecular (black), H–O intermolecular (red), H–O intramolecular (green). (b) O–P intermolecular (black), O–P intramolecular (red), O–O intermolecular (green), O–O intramolecular (blue). (c) H–H total (black), H–H intermolecular (red), H–H intramolecular (green). [Color figure can be viewed in the online issue, which is available at wileyonlinelibrary.com.]

3.2.2. Solubility Parameter

As listed in Table V, the solubility parameters of PA at 298, 333, 393, 423, and 453 K were calculated to be 44.65, 43.28, 39.48, 38.26, and 34.62 $\text{MPa}^{1/2}$, respectively. Unfortunately, no experimental values of the solubility parameter have been reported for PA in the literature thus far. But as the solubility parameter of water is known to be 47.9 $\text{MPa}^{1/2}$ at 298 K [42], another MD simulation was carried out on a 125-molecule water cell at 298 K using the same settings and procedure as for PA. The simulated solubility parameter of water is 48.12 $\text{MPa}^{1/2}$, which agrees well with the experimental value of 47.9 $\text{MPa}^{1/2}$ [41].

3.2.3. RDFS

Figure 7 presents the schematic RDFs for all atom-atom pairs determined at 298 and 333 K. The peak positions for these functions are summarized in Table VI, and are also compared with neutron diffraction results [10] determined at 300 K and RDF results obtained from an AIMD study at 333 K by Tsuchida [13]. Table V exhibits the RDF results calculated using COMPASS agree well with the AIMD and neutron diffraction results.

Specifically, Figure 7(a) contains RDFs for intramolecular H–O, intermolecular H–O and intramolecular H–P pairs determined at 298 and 333 K, respectively. For RDFs of the intramolecular H–O pair, the first peak at $r = 0.95 \text{ Å}$ for both 298 and 333 K corresponds to the H–O covalent bond. The second peak at $r = 1.49 \text{ Å}$ for 298 K, and $r = 1.47 \text{ Å}$ for 333 K, suggests that the H–O covalent bond is elongated because of the formation of intermolecular hydrogen bonding ($\text{O} \cdots \text{H} \cdots \text{O}$) next to it. The appearance of this peak is probably because COMPASS cannot describe bond breaking and formation. This peak does not exist in neutron diffraction and AIMD results. The double peaks between 2.5 and 3.5 Å are between an H atom on the one side and the three O atoms on the other side of the PO_4 tetrahedron [10]. The double peaks indicate that these three O atoms are not equivalent [10]. RDFs for the intermolecular H–O pair show peaks at 1.53 and 1.55 Å, for 298 and 333 K, respectively, which can be attributed to the strong intermolecular hydrogen bonds. RDFs for the intramolecular H–P pair show peaks at around 2.00 Å.

Figure 7(b) includes RDFs for intramolecular and intermolecular correlations for both P–O and

TABLE VI

RDF results for the 125-molecule PA cell using COMPASS at 298 K and 333 K, compared with neutron diffraction results obtained at 300 K and RDF results obtained from an AIMD study at 333 K.

Assignment	Position (Å)			
	125 PA 298 K	125 PA 333 K	Neutron diffraction 300 K ^a	AIMD 333 K ^b
H—O direct bond	0.95	0.95	0.98	1.00
H—O intramolecular	1.49	1.47	—	—
H—O through hydrogen bond	1.53	1.55	1.54	1.55–1.60
H—P intramolecular	2.01	1.99	2.20	2.20
H—O2 intramolecular	2.57	2.61	2.80	2.85
H—O3/4 intramolecular	3.19	3.23	3.25	3.35
O—P direct bond	1.55	1.55	1.54	1.55
O—O intramolecular	1.77	1.79	—	—
O—O intramolecular and through hydrogen bond	2.53	2.49–2.55	2.51	2.50–2.55
O—P intermolecular	3.67–3.77	3.75	3.7	3.60–3.70
O—O intermolecular	4.69	4.71	4.9	4.85–4.90
O—P intermolecular	5.45	5.43	5.6	5.65
O—O intermolecular	7.11	7.11	7.1	7.15
H—H across hydrogen bond	2.13–2.27	2.17–2.33	1.9–2.6	2.40–2.45
H—H intramolecular and intermolecular	2.69 ^c	2.61 ^c	2.5–4.2	3.55–3.65

^aNeutron diffraction results obtained at 300 K, Ref. [10].

^bRDFs determined at 333 K from an AIMD study by Tsuchida, Ref. [13].

^cFor H—H intramolecular only; no peak was found for H—H intermolecular near this position.

O—O pairs. The intramolecular correlation between P and O atoms show a single high peak at 1.55 Å at both 298 and 333 K. It indicates that the single and double bonds between P and O atoms are indistinguishable in both gas and liquid states. The RDF for the intramolecular O—O pair shows two peaks at 1.77 and 2.53 Å at 298 K. It describes the correlation between an O atom on the one side and the other three O atoms on the other side in the PO₄ tetrahedron. However, the peak at 1.77 Å corresponds to a weak correlation and it does not appear in the neutron diffraction and AIMD results. Besides, the RDF for the intermolecular O—O pair also shows peak at 2.53 Å at 298 K, which describes the intermolecular hydrogen bonding. RDFs determined at 333 K are similar to those calculated at 298 K, and can be understood the same way. Other peak positions for intermolecular O—O pair and O—P pair are listed in Table V.

Figure 7(c) describes the H—H correlation. It can be seen that RDFs for the intermolecular correlation show peaks at 2.13–2.27 Å and 2.17–2.33 Å, for 298 and 333 K, respectively. It describes the H—H pair across hydrogen bond (O—H···O).

RDFs for the intramolecular correlation show peaks at 2.69 and 2.61 Å, for 298 and 333 K, respectively. In the neutron diffraction and AIMD results, the intermolecular H—H pair also shows weak peaks between 2.5 and 4.2 Å, which are not shown in the RDFs determined using COMPASS.

Figure 8 illustrates the schematic RDFs for all atom-atom pairs determined at 298 and 453 K to further probe the effect of temperature on the RDFs. Plots in Figure 8 displays most RDFs have broader distributions as temperature increases. This is probably because pure PA in the condensed phase is dominated by a three-dimensional short hydrogen bond (~2.5 Å) network, and such strong hydrogen-bonded system is expected to have significant temperature dependence in structure and vibrational properties, which has been understood using AIMD by Iyengar et al. [43, 44]. Besides, Figure 8 also presents a trend that the heights of peaks for intramolecular correlations increase as temperature, accompanied by the decreases of peak heights for intermolecular correlations. For examples, at 453 K, Figure 8(a) shows the peak height for the H—O intramolecular correlation at 1.45 Å rises from 0.4 to 1.5

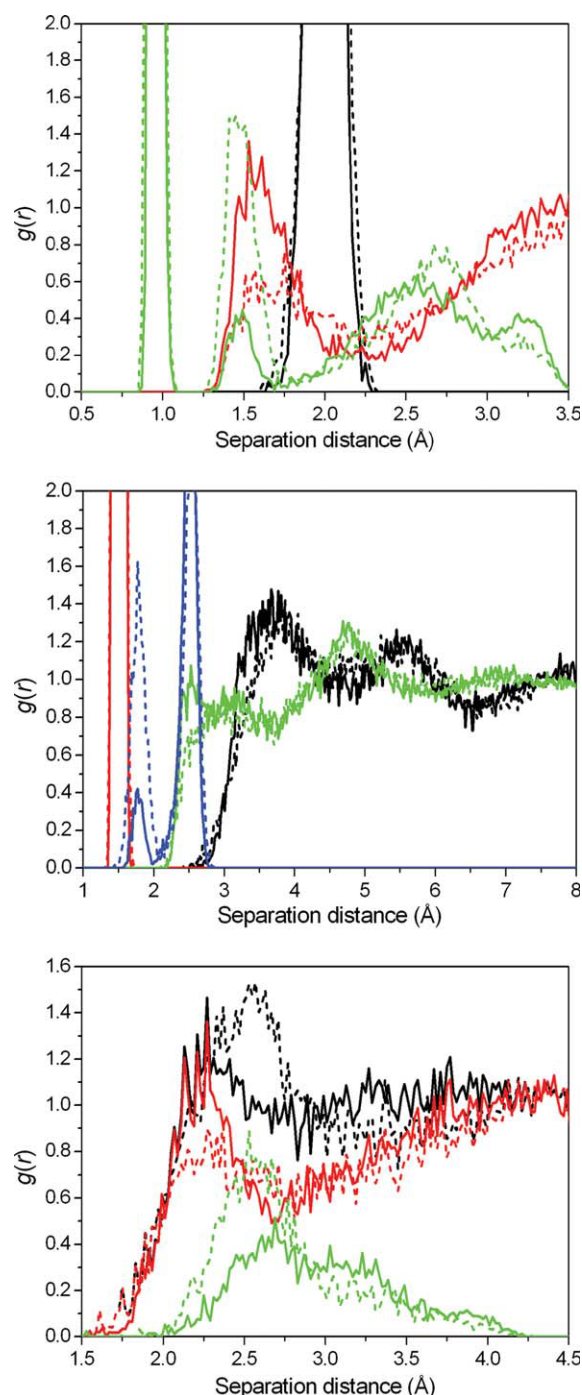


FIGURE 8. The schematic RDFs $g(r)$ for all atom-atom pairs determined at 298 K (full line) and at 453 K (short dashed line). (a) P—H intramolecular (black), H—O intermolecular (red), H—O intramolecular (green). (b) O—P intermolecular (black), O—P intramolecular (red), O—O intermolecular (green), O—O intramolecular (blue). (c) H—H total (black), H—H intermolecular (red), H—H intramolecular (green). [Color figure can be viewed in the online issue, which is available at wileyonlinelibrary.com.]

and that for H—O intermolecular correlation at 1.55 Å drops from 1.35 to 0.7; In Figure 8(b), the height of peak for the O—O intramolecular correlation at 1.8 Å increases from 0.4 to 1.6; Figure 8(c) also displays the peak height for the H—H intermolecular correlation at 2.25 Å drops with the increases of the peak height for the H—H intramolecular correlation.

RDFs for the two kinds of intermolecular hydrogen bonds (H···O—H and H···O=P) in PA at different temperatures are also calculated. Results are presented in Figure S5 of the Supporting Information and summarized in Table VII. By comparing the lengths of the two hydrogen bonds (e.g., 1.65 Å for H···O=P and 1.53 Å for H···O—H at 298 K), it can be concluded that the interaction between H···O=P is stronger than that between H···O—H. As for the effects of temperature on the two kinds of hydrogen bonds, the results show a general trend that lengths of both hydrogen bonds increase with the temperature, and at the same time, the intensities decrease. Besides, the broader distribution of RDFs at increased temperatures is testified again in Figure S5, and even more visually intuitive than that in Figure 8.

3.2.4. Self-Diffusion Coefficients and Activation Energy

As the COMPASS force field cannot describe bond-breaking/bond-making events, nor the fast PT processes, only the self-diffusion coefficients of P atoms obtained using COMPASS, together with the self-diffusion coefficients of P and H atoms attained by PFG-NMR, are plotted in Figure 9. It can be seen that the calculated self-diffusion coefficients of P atoms are a little larger than those determined by PFG-NMR, and the differences become smaller as temperature increases. At 393 K, the simulated self-diffusion coefficient of P

TABLE VII
The highest RDF peaks for the two kinds of hydrogen bonding.

	H···O=P		H···O—H	
	Distance (Å)	$g_{\text{H-O}}$ (r)	Distance (Å)	$g_{\text{H-O}}$ (r)
298 K	1.65	1.26	1.53	1.66
333 K	1.71	1.24	1.55	1.40
393 K	1.71	1.13	1.57	1.10
423 K	1.57–1.89	0.84	1.57	1.04
453 K	1.85	1.03	1.57–1.75	0.83

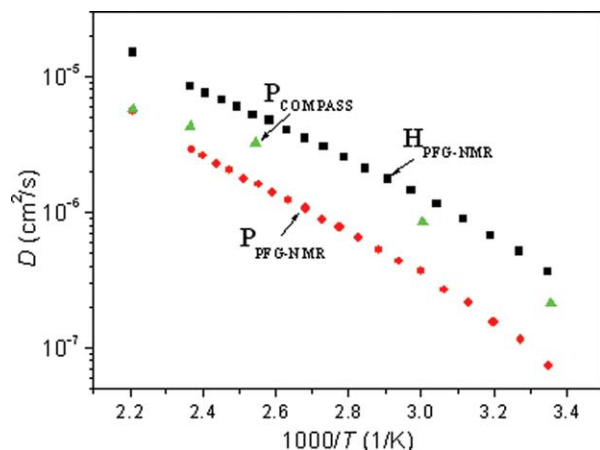


FIGURE 9. Self-diffusion coefficients at different temperatures, obtained using the COMPASS force field and by the PFG-NMR technique, respectively. For $H_{\text{PFG-NMR}}$ and $P_{\text{PFG-NMR}}$, the two points at 453 K are predicted by extrapolation. [Color figure can be viewed in the online issue, which is available at wileyonlinelibrary.com.]

atoms is $3.26 \times 10^{-6} \text{ cm}^2/\text{s}$, which agrees with the PFG-NMR result within a factor of 2. At 453 K, the calculated self-diffusion coefficient of P

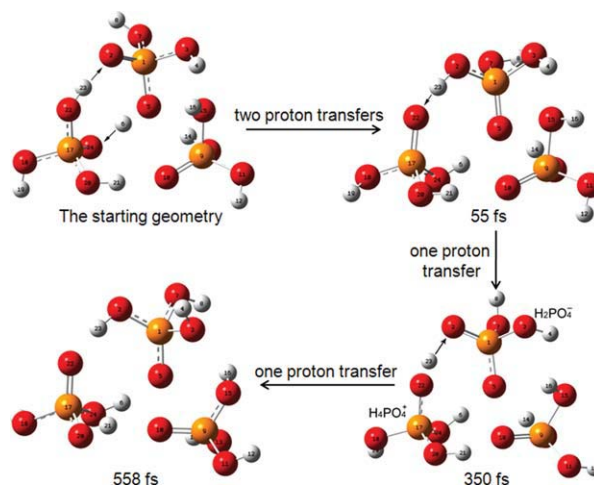


FIGURE 10. Typical snapshots during the 1-ps ADMP simulation. [Color figure can be viewed in the online issue, which is available at wileyonlinelibrary.com.]

atoms is $5.77 \text{ cm}^2/\text{s}$, which is only 3% higher than the extrapolated experimental result. The calculated activation energy E_a , according to Eq. (8), is 23.81 kJ/mol, which shows an acceptable

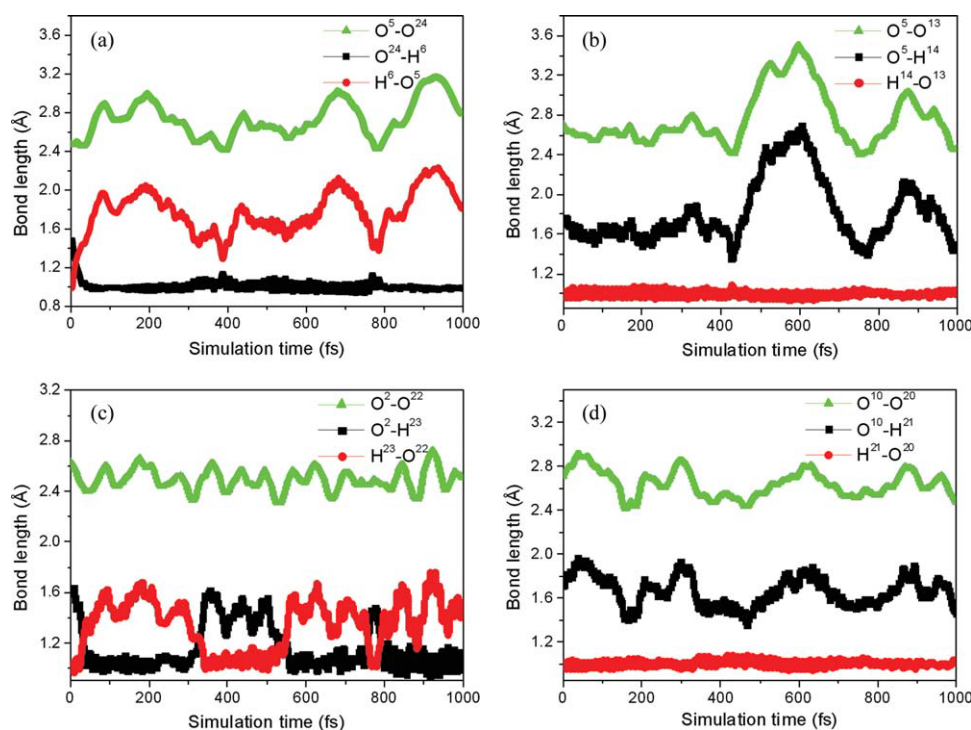


FIGURE 11. Structural parameter for four intermolecular hydrogen bonds ($\text{O}-\text{H}\cdots\text{O}=\text{P}$) in the three-molecule PA cluster during the 1-ps ADMP simulation. [Color figure can be viewed in the online issue, which is available at wileyonlinelibrary.com.]

difference ($\sim 20\%$) from the PFG-NMR result of 29.77 kJ/mol [3].

3.3. ADMP

Several typical snapshots during the 1-ps ADMP simulations are shown in Figure 10. Figure 11 presents the variations of bond lengths with simulation time for all four intermolecular hydrogen bonds of "O—H...O=P" between these PA molecules. Plots in Figure 11 predict the length of hydrogen bond to be ~ 1.6 Å and the length of intramolecular O—H bond as ~ 1.0 Å, which agree well with neutron diffraction [10] and the COMPASS results. As shown by Figures 10 and 11(a, b), mutual two PTs between two PA molecules occurred at the very beginning of the simulation. A fast self-dissociation process in PA, as depicted by Reaction (1), occurred between 350 and 550 fs. Figures 11(a) and (b) also suggests that protons tried to make another transfer at ~ 770 fs, but they did not succeed. Figures 11(c) and (d) do not show evidences for PT between other PA-PA pairs. It can be seen that the variations of the lengths of hydrogen bonds are accompanied by changes of the lengths of intermolecular O—O distances, but without breaking of the intramolecular O—H covalent bond.

4. Conclusions

In this study, we have used a combination of QM, MD, and ADMP methods to study PA. On the basis of the results obtained from our calculations, the following conclusions are made.

Calculated proton affinities using B3LYP/6-31++G(d,p), with ZPE and thermal enthalpies corrections, in descending order are (unit: kJ/mol): $\text{P}_2\text{O}_7^{4-}$ (2584.45) > PO_4^{3-} (2404.41) > $\text{HP}_2\text{O}_7^{3-}$ (2165.65, 2091.78) > HPO_4^{2-} (1892.42) > $\text{H}_2\text{P}_2\text{O}_7^{2-}$ (1667.06, 1740.93) > H_2PO_4^- (1359.76) > $\text{H}_3\text{P}_2\text{O}_7^-$ (1242.38) > $\text{H}_4\text{P}_2\text{O}_7$ (857.45) > H_3PO_4 (822.43) > H_2O (684.12) > $\text{H}_5\text{P}_2\text{O}_7^+$ (434.85). The larger the proton affinity, the more prone a component is to associate a proton.

Calculated interaction energies for PPA-PA, PPA-water, PA-PA, and PA-water with B3LYP/6-31++G(d,p) are 129.56, 86.21, 84.70, and 38.35 kJ/mol, respectively. The larger the interaction energy, the more prone are the molecules to form hydrogen-bonded molecular pair.

Determined energy barrier heights for different PT pathways, using the SCD and QST3 techniques,

in ascending order are (unit: kJ/mol): $\text{H}_3\text{O}^+ \rightarrow \text{H}_3\text{PO}_4$ (0); $\text{H}_4\text{P}_2\text{O}_7 \rightarrow \text{H}_3\text{PO}_4$ (2.61); $\text{H}_3\text{PO}_4 \rightarrow \text{H}_2\text{PO}_4^-$ (5.31); $\text{H}_4\text{PO}_4^+ \rightarrow \text{H}_3\text{PO}_4$ (~ 7.33); $\text{H}_3\text{PO}_4 \rightarrow \text{H}_4\text{P}_2\text{O}_7/\text{H}_3\text{PO}_4 \rightarrow \text{H}_3\text{PO}_4$ (15.99); $\text{H}_4\text{P}_2\text{O}_7 \rightarrow \text{H}_2\text{O}$ (28.61); $\text{H}_3\text{PO}_4 \rightarrow \text{H}_2\text{O}$ (47.14). Generally, the lower the energy barrier, the easier PT can occur.

The good agreement of density, RDFs, self-diffusion coefficient and activation energy with experimental and AIMD results at different temperatures shows that COMPASS is an acceptable force field for PA studies.

Results of preliminary ADMP studies on a cluster of three PA molecules indicate that ADMP can reasonably describe PT and self-dissociation processes in the PA system.

ACKNOWLEDGMENTS

The authors thank Ohio Supercomputer Center for allocation of computing time. Acknowledgment is made to the donors of the American Chemical Society Petroleum Research Fund for partial support of this research.

References

- Pauling, L. General Chemistry, 3rd Ed.; W. H. Freeman and Company: San Francisco; 1970.
- Toy, A. D. F.; Walsh, E. N. Phosphorus Chemistry in Everyday living, 2nd Ed.; American Chemical Society: Washington, DC; 1987.
- Dippel, T.; Kreuer, K. D.; Lassegues, J. C.; Rodriguez, D. Solid State Ionics 1993, 61, 41.
- Kreuer, K. D.; Paddison, S. J.; Spohr, E.; Schuster, M. Chem Rev 2004, 104, 4637.
- Wainright, J. S.; Wang, J. T.; Wang, D.; Savinell, R.; Litt, M. J Electrochem Soc 1995, 142, L121.
- Ma, Y. L.; Wainright, J. S.; Litt, M. H.; Savinell, R. F. J Electrochem Soc 2004, 151, A8.
- Munson, R. A. J Phys Chem 1964, 68, 3374.
- Greenwood, N. N.; Thompson, A. J Chem Soc 1959, 1959, 3485.
- Egan, E. P.; Luff, B. B. Ind Eng Chem 1955, 47, 1280.
- Tromp, R. H.; Spieser, S. H.; Neilson, G. W. J Chem Phys 1999, 110, 2145.
- Moss, G. R.; Souhassou, M.; Blessing, R. H.; Espinosa, E.; Lecomte, C. Acta Crystallogr B 1995, 51, 650.
- Spieser, S. A. H.; Leeftang, B. R.; Kroon-Batenburg, L. M. J.; Kroon, J. J Phys Chem A 2000, 104, 7333.
- Tsuchida, E. J Phys Soc Jpn 2006, 75, 054801.
- Sun, H. J Phys Chem B 1998, 102, 7338.
- Sun, H.; Ren, P.; Fried, J. Comput Theor Polym Sci 1998, 8, 229.
- Schlegel, B. H.; Millam, J. M.; Iyengar, S. S.; Voth, G. A.; Daniels, A. D.; Scuseria, G. E.; Frisch, M. J. J Chem Phys 2001, 114, 9758.

17. Iyengar, S. S.; Schlegel, B. H.; Millam, J. M.; Voth, G. A.; Scuseria, G. E.; Frisch, M. J. *J Chem Phys* 2001, 115, 10291.
18. Schlegel, B. H.; Iyengar, S. S.; Li, X.; Millam, J. M.; Voth, G. A.; Scuseria, G. E.; Frisch, M. J. *J Chem Phys* 2002, 117, 8694.
19. Iyengar, S. S.; Schlegel, H. B.; Voth, G. A.; Millam, J. M.; Scuseria, G. E.; Frisch, M. J. *Isr J Chem* 2002, 42, 191.
20. Iyengar, S. S.; Schlegel, H. B.; Voth, G. A. *J Phys Chem A* 2003, 107, 7269.
21. Iyengar, S. S.; Frisch, M. J. *J Chem Phys* 2004, 121, 5061.
22. Rega, N.; Iyengar, S. S.; Voth, G. A.; Schlegel, H. B.; Vreven, T.; Frisch, M. J. *J Phys Chem B* 2004, 108, 4210.
23. Frisch, M. J.; Trucks, G. W.; Schlegel, H. B.; Scuseria, G. E.; Robb, M. A.; Cheeseman, J. R.; Montgomery, J., J. A.; Vreven, T.; Kudin, K. N.; Burant, J. C.; Millam, J. M.; Iyengar, S. S.; Tomasi, J.; Barone, V.; Mennucci, B.; Cossi, M.; Scalmani, G.; Rega, N.; Petersson, G. A.; Nakatsuji, H.; Hada, M.; Ehara, M.; Toyota, K.; Fukuda, R.; Hasegawa, J.; Ishida, M.; Nakajima, T.; Honda, Y.; Kitao, O.; Nakai, H.; Klene, M.; Li, X.; Knox, J. E.; Hratchian, H. P.; Cross, J. B.; Bakken, V.; Adamo, C.; Jaramillo, J.; Gomperts, R.; Stratmann, R. E.; Yazyev, O.; Austin, A. J.; Cammi, R.; Pomelli, C.; Ochterski, J. W.; Ayala, P. Y.; Morokuma, K.; Voth, G. A.; Salvador, P.; Dannenberg, J. J.; Zakrzewski, V. G.; Dapprich, S.; Daniels, A. D.; Strain, M. C.; Farkas, O.; Malick, D. K.; Rabuck, A. D.; Raghavachari, K.; Foresman, J. B.; Ortiz, J. V.; Cui, Q.; Baboul, A. G.; Clifford, S.; Cioslowski, J.; Stefanov, B. B.; Liu, G.; Liashenko, A.; Piskorz, P.; Komaromi, I.; Martin, R. L.; Fox, D. J.; Keith, T.; Al-Laham, M. A.; Peng, C. Y.; Nanayakkara, A.; Challacombe, M.; Gill, P. M. W.; Johnson, B.; Chen, W.; Wong, M. W.; Gonzalez, C.; Pople, J. A. *Gaussian 03, Revision C. 02*; Gaussian, Inc.: Wallingford, CT, 2004.
24. McNaught, A. D.; Wilkinson, A. *Compendium of Chemical Terminology*, 2nd Ed.; Blackwell Scientific Publications: Oxford, 1997.
25. Einstein, A.; Stern, O. *Ann Phys (Leipzig)* 1913, 40, 551.
26. Ochterski, J. W. *Thermochemistry in Gaussian*; Gaussian, Inc.: Wallingford, CT, 2000.
27. van Duijneveldt, F. B.; van Duijneveldt-van de Rijdt, J. G. C. M.; van Lenthe, J. H. *Chem Rev* 1994, 94, 1873.
28. Young, D. *Computational Chemistry. A Practical Guide for Applying Techniques to Real World Problems*; Wiley: New York, 2001.
29. Peng, C.; Ayala, P. Y.; Schlegel, H. B.; Frisch, M. J. *J Comp Chem* 1996, 17, 49.
30. Peng, C.; Schlegel, H. B. *Isr J Chem* 1994, 33, 449.
31. Dewar, M. J. S.; Kirschner, S. *J Am Chem Soc* 1971, 93, 4292.
32. *Materials Studio 4.3*, Accelrys Software Inc.: San Diego, 2008.
33. Lifson, S.; Hagler, A. T.; Dauber, P. *J Am Chem Soc* 1979, 101, 5111.
34. Sun, H.; Mumby, S. J.; Maple, J. R.; Hagler, A. T. *J Phys Chem* 1995, 99, 5873.
35. Andersen, H. C. *J Chem Phys* 1980, 72, 2384.
36. Berendsen, H. J. C.; Postma, J. P. M.; van Gunsteren, W. F.; DiNola, A.; Haak, J. R. *J Chem Phys* 1984, 81, 3684.
37. Ewald, P. P. *Ann Phys (Leipzig)* 1921, 64, 253.
38. Einstein, A. *Ann Phys (Leipzig)* 1905, 322, 549.
39. Trohalaki, S.; Kloczkowski, A.; Mark, J. E.; Rigby, D.; Roe, R. J. *Computer Simulation of Polymers*; Prentice Hall: Englewood Cliffs, NJ, 1991; p 220.
40. Car, R.; Parrinello, M. *Phys Rev Lett* 1985, 55, 2471.
41. Linstrom, P. J.; Mallard, W. G. *NIST Chemistry WebBook*; NIST Standard Reference Database No. 69; National Institute of Standards and Technology: Gaithersburg, MD, 2003 (<http://webbook.nist.gov>).
42. Burrell, H. *Encyclopedia of Polymer Science and Technology*, 2nd Ed.; Wiley: New York, 1970; Chapter 2.
43. Li, X.; Moore, D. T.; Iyengar, S. S. *J Chem Phys* 2008, 128, 184308.
44. Sumner, I.; Iyengar, S. S. *J Phys Chem A* 2007, 111, 10313.